





















Shedding New Light on Weak Emission-Line Quasars in the C IV–H β Parameter Space

TRUNG HA ¹, COOPER DIX ¹, BRANDON M. MATTHEWS ¹, OHAD SHEMMER ¹, MICHAEL S. BROTHERTON ²,
ADAM D. MYERS², GORDON T. RICHARDS ³, JAYA MAITHIL ⁴, SCOTT F. ANDERSON ⁵, W. N. BRANDT ^{6,7,8},
ALEKSANDAR M. DIAMOND-STANIC⁹, XIAOHUI FAN ¹⁰, S. C. GALLAGHER ¹¹, RICHARD GREEN ¹⁰, PAULINA LIRA¹²,
BIN LUO ^{13,14}, HAGAI NETZER ¹⁵, RICHARD M. PLOTKIN ^{16,17}, JESSIE C. RUNNOE ¹⁸, DONALD P. SCHNEIDER ^{6,7},
MICHAEL A. STRAUSS ¹⁹, BENNY TRAKHTENBROT ¹⁵ AND JIANFENG WU ²⁰

¹*Department of Physics, University of North Texas, Denton, TX 76203, USA*

²*Department of Physics and Astronomy, University of Wyoming, Laramie, WY 82071, USA*

³*Department of Physics, Drexel University, 32 S 32nd St., Philadelphia, PA 19104, USA*

⁴*Center for Astrophysics | Harvard & Smithsonian, 60 Garden Street, Cambridge, MA 02138, USA*

⁵*Department of Astronomy, University of Washington, Box 351580, Seattle, WA 98195, USA*

⁶*Department of Astronomy and Astrophysics, The Pennsylvania State University, University Park, PA 16802, USA*

⁷*Institute for Gravitation and the Cosmos, The Pennsylvania State University, University Park, PA 16802, USA*

⁸*Department of Physics, 104 Davey Lab, The Pennsylvania State University, University Park, PA 16802, USA*

⁹*Department of Physics and Astronomy, Bates College, Lewiston, ME, 04240, USA*

¹⁰*Steward Observatory, University of Arizona, 933 North Cherry Avenue, Tucson, AZ 85721, USA*

¹¹*Department of Physics and Astronomy, University of Western Ontario, 1151 Richmond St, London, ON N6C 1T7, Canada*

¹²*Departamento de Astronomía, Universidad de Chile, Casilla 36D, Santiago, Chile*

¹³*School of Astronomy and Space Science, Nanjing University, Nanjing, Jiangsu 210093, People's Republic of China*

¹⁴*Key Laboratory of Modern Astronomy and Astrophysics (Nanjing University), Ministry of Education, Nanjing, Jiangsu 210093, People's Republic of China*

¹⁵*School of Physics and Astronomy, Tel Aviv University, Tel Aviv 69978, Israel*

¹⁶*Department of Physics, University of Nevada, Reno, NV 89557, USA*

¹⁷*Nevada Center for Astrophysics, University of Nevada, Las Vegas, NV 89154, USA*

¹⁸*Department of Physics and Astronomy, Vanderbilt University, Nashville, TN 37235, USA*

¹⁹*Department of Astrophysical Sciences, Princeton University, Princeton, NJ 08544, USA*

²⁰*Department of Astronomy, Xiamen University, Xiamen, Fujian 361005, People's Republic of China*

(Received December 1, 2022; Revised March 19, 2023; Accepted April 9, 2023)

ABSTRACT

Weak emission-line quasars (WLQs) are a subset of Type 1 quasars that exhibit extremely weak Ly α +N V λ 1240 and/or C IV λ 1549 emission lines. We investigate the relationship between emission-line properties and accretion rate for a sample of 230 ‘ordinary’ Type 1 quasars and 18 WLQs at $z < 0.5$ and $1.5 < z < 3.5$ that have rest-frame ultraviolet and optical spectral measurements. We apply a correction to the H β -based black-hole mass (M_{BH}) estimates of these quasars using the strength of the optical Fe II emission. We confirm previous findings that WLQs’ M_{BH} values are overestimated by up to an order of magnitude using the traditional broad emission-line region size-luminosity relation. With this M_{BH} correction, we find a significant correlation between H β -based Eddington luminosity ratios and a combination of the rest-frame C IV equivalent width and C IV blueshift with respect to the systemic redshift. This correlation holds for both ordinary quasars and WLQs, which suggests that the two-dimensional C IV parameter space can serve as an indicator of accretion rate in all Type 1 quasars across a wide range of spectral properties.

Keywords: galaxies: active — quasars: emission line — quasars: weak emission-line

1. INTRODUCTION

Weak emission-line quasars (WLQs) are a subset of Active Galactic Nuclei (AGN) with extremely weak or undetectable rest-frame UV emission lines (e.g., Fan et al. 1999; Anderson et al. 2001; Collinge et al. 2005; Plotkin et al. 2010). The Sloan Digital Sky Survey (SDSS; York et al. 2000) has discovered $\approx 10^3$ Type 1 quasars with Ly α +N V λ 1240 rest-frame equivalent width (EW) $< 15.4 \text{ \AA}$ and/or C IV λ 1549 EW $< 10.0 \text{ \AA}$ (e.g., Diamond-Stanic et al. 2009; Meusinger & Balafkan 2014). These numbers represent a highly significant concentration of quasars at $\gtrsim 3\sigma$ deviation from the log-normal EW distribution of the SDSS quasar population, with no corresponding ‘tail’ at the opposite end of the distribution (Diamond-Stanic et al. 2009; Wu et al. 2012). Furthermore, the fraction of WLQs among the broader quasar population increases sharply at higher redshifts (and thus higher luminosities), from $\sim 0.1\%$ at $3 \lesssim z \lesssim 5$ to $\sim 10\text{--}15\%$ at $z \gtrsim 5.7$ (Diamond-Stanic et al. 2009; Bañados et al. 2016; Shen et al. 2019).

Multi-wavelength observations of sources of this class have shown that they are unlikely to be high-redshift galaxies with apparent quasar-like luminosity due to gravitational-lensing amplification, dust-obscured quasars, or broad-absorption-line (BAL) quasars (e.g., Shemmer et al. 2006, 2010), but that their UV emission-lines are intrinsically weak. Furthermore, WLQs are typically radio-quiet, and have X-ray and mid-infrared properties inconsistent with those of BL Lac objects (Shemmer et al. 2009; Lane et al. 2011; Wu et al. 2012; Massaro et al. 2017).

About half of WLQs have notably lower X-ray luminosities than expected from their monochromatic luminosities at 2500 \AA (e.g., Luo et al. 2015; Ni et al. 2018, 2022; Timlin et al. 2020). One explanation for this phenomenon is that, at small radii, the geometrically thick accretion disks of these WLQs are ‘puffed up’ and prevent highly ionizing photons from reaching the broad emission-line region (BELR; e.g. Wu et al. 2011, 2012; Luo et al. 2015; Ni et al. 2018, 2022). The X-ray radiation is partially absorbed by the thick disk, resulting in low apparent X-ray luminosities at high inclinations (i.e., when these objects are viewed edge-on). When these objects are viewed at much lower inclinations, their notably steep X-ray spectra indicate accretion at high Eddington luminosity ratio ($L_{\text{bol}}/L_{\text{Edd}}$, hereafter L/L_{Edd} ; e.g., Shemmer et al. 2008; Luo et al. 2015; Marlar et al. 2018).

The indications of high Eddington ratios in WLQs may provide a natural explanation for the weakness of their emission lines in the context of the Baldwin Effect. In its classical form, this effect is an anti-correlation between the EW(C IV) and the quasar luminosity (Baldwin 1977). Subsequent studies, however, have found that this relation stems from a more fundamental anti-correlation between EW(C IV) and H β -based L/L_{Edd} (Baskin & Laor 2004, hereafter BL04; Dong et al. 2009). This anti-correlation, coined the Modified Baldwin Effect (MBE), was extensively studied and built upon by Shemmer & Lieber (2015, hereafter SL15) (however, see also Wang et al. 2022). SL15 utilized a sample of nine WLQs and 99 non-radio-loud, non-BAL (‘ordinary’) quasars spanning wide ranges of luminosity and redshift to analyze the relative strength of the C IV emission-line and the H β -based Eddington ratio. They confirmed the findings of BL04 for the sample of ordinary quasars. However, all nine WLQs were found to possess relatively low L/L_{Edd} values, while the MBE predicts considerably higher Eddington ratios for these sources. This finding led SL15 to conclude that the H β -based L/L_{Edd} parameter cannot depend solely on EW(C IV) for all quasars. Such a conclusion may also be consistent with subsequent findings that WLQs possess strong Fe II emission and large velocity offsets of the C IV emission-line peak with respect to the systemic redshift (hereafter, Blueshift(C IV)) (Martínez-Aldama et al. 2018), and that L/L_{Edd} correlates with Blueshift(C IV) at high Blueshift(C IV) values (see Figure 14 of Rankine et al. 2020).

In this work, we explore two possible explanations for the findings of SL15. The first of these is that the traditional estimation of H β -based black-hole mass (M_{BH}) values, and therefore L/L_{Edd} values, fails to accurately predict M_{BH} , particularly in quasars with strong optical Fe II emission (e.g., Shen 2013; Maithil et al. 2022). Such a case is typical for WLQs, and thus a correction via measurement of the strength of the Fe II emission-complex in the optical band is required (Du & Wang 2019; Yu et al. 2020b). The second explanation is that EW(C IV), by itself, is not an ideal indicator of the quasar accretion rate. In addition to EW(C IV), we utilize a recently defined parameter, the ‘C IV || Distance’ (Rivera et al. 2022, hereafter R22), which represents a combination of the EW(C IV) and Blueshift(C IV) (Richards et al. 2011; Rivera et al. 2020; McCaffrey &

Richards 2021), and search for a correlation between that parameter and L/L_{Edd} .

To investigate these explanations, we extend the WLQ sample of SL15 to nine additional sources available from the Gemini Near-IR Spectrograph - Distant Quasar Survey (GNIRS-DQS; Matthews et al. 2023, under review, hereafter Paper I). Furthermore, we study the distribution of WLQs in L/L_{Edd} space versus a sample of ordinary quasars from SL15 and Paper I. We aim to investigate the underlying driver for the weak emission lines in WLQs and test the assertion that all WLQs have extremely high accretion rates.

The structure of this paper is as follows. In Section 2, we discuss our sample selection and the relevant equations used to estimate $H\beta$ -based L/L_{Edd} values. In Section 3, we analyze the samples' spectroscopic properties as well as the sources' black-hole masses and accretion rates. Subsequently, we discuss the correlation between the C IV parameter space and L/L_{Edd} . In Section 4, we summarize our findings. Throughout this paper, we compute luminosity distances using a standard Λ CDM cosmology with $H_0 = 70 \text{ km s}^{-1} \text{ Mpc}^{-1}$, $\Omega_{\text{M}} = 0.3$, and $\Omega_{\Lambda} = 0.7$ (e.g., Spergel et al. 2007).

2. SAMPLE SELECTION AND DATA ANALYSIS

2.1. WLQ Sample

We compile a sample of 18 WLQs that have accurate full-width-at-half-maximum intensity of the broad component of the $H\beta$ $\lambda 4861$ emission line (hereafter, $\text{FWHM}(H\beta)$), monochromatic luminosity at rest-frame 5100 \AA (hereafter, $\nu L_{\nu}(5100 \text{ \AA})$), $\text{EW}(\text{Fe II } \lambda\lambda 4434 - 4684)$, and $\text{EW}(H\beta)$ measurements. Nine of these sources were obtained from SL15, seven from the GNIRS-DQS sample of Paper I (see Section 2.2), and two from this work (see Appendix A). SL15 compiled a sample of nine WLQs: SDSS J0836+1425, SDSS J1411+1402, SDSS J1417+0733, SDSS J1447-0203 (Plotkin et al. 2010; Plotkin et al. 2015), SDSS J0945+1009 (Hryniewicz et al. 2010; Plotkin et al. 2015), SDSS J1141+0219, SDSS J1237+6301 (Diamond-Stanic et al. 2009; Shemmer et al. 2010), SDSS J1521+5202 (Just et al. 2007; Wu et al. 2011), and PHL 1811 (Leighly et al. 2007).

Table 1 provides basic properties for the 18 WLQs in our sample. Column (1) provides the source name; Column (2) gives the systemic redshift determined from the peak of, in order of preference, the [O III] $\lambda 5007$, Mg II $\lambda 2798$, and $H\beta$ emission lines; Column (3) gives $\log \nu L_{\nu}(5100 \text{ \AA})$; Column (4) gives $\text{FWHM}(H\beta)$; Column (5) gives $R_{\text{Fe II}} \approx \text{EW}(\text{Fe II})/\text{EW}(H\beta)$; Column (6) gives traditional $H\beta$ -based M_{BH} estimates (following Equations 2 and 4); Column (7) gives Fe II-corrected $H\beta$ -

based $M_{\text{BH, corr}}$ estimates (following Equations 3 and 4); Column (8) gives traditional $H\beta$ -based L/L_{Edd} values (from Equation 5); Column (9) gives Fe II-corrected $H\beta$ -based $L/L_{\text{Edd, corr}}$ values (from Equation 5); Column (10) gives $\text{EW}(\text{C IV})$; Column (11) gives $\text{Blueshift}(\text{C IV})$; Columns (12) and (13) provide the references for the rest-frame optical and UV spectral measurements, respectively. All derived properties are discussed in detail in Section 2.4.

The two WLQs from Shemmer et al. (2010) and the two introduced in Appendix A do not have a reliable C IV line measurement in the literature, hence we perform our own measurements from their SDSS spectra, following the procedure in Dix et al. (2023, hereafter Paper II). Briefly, we fit the C IV emission line with a local, linear continuum and two independent Gaussians. These Gaussians are constrained such that the flux densities lie between 0 and twice the value of the peak of the emission line; the FWHM is restricted to not exceed 15000 km s^{-1} . Furthermore, we visually inspect the initial fit to correct for any additional residuals. The EW of the line emission can then be measured, as well as the blueshift, which is calculated from the difference between $\lambda 1549$ and the rest-frame wavelength of the peak of the emission-line profile (see Equation 1).

Our WLQs appear to possess stronger relative optical Fe II emission (indicated by the larger $R_{\text{Fe II}}$ values) compared to ordinary quasars from their respective samples. Since such sources are selected based only on their C IV emission-line strength ($\text{EW}(\text{C IV}) < 10 \text{ \AA}$), we are unable to assess any potential biases introduced by the rest-frame optical emission to their selection process.

2.2. Ordinary Quasar Sample Selection

In order to create a comprehensive comparison sample of quasars for our analysis, which requires measurements of both the $H\beta$ and C IV emission lines, we select two catalogs of ordinary quasars from the literature. For the high-redshift quasars ($1.5 \lesssim z \lesssim 3.5$), C IV emission properties can be obtained from SDSS, but the $H\beta$ emission line lies outside of the SDSS range, and therefore it has to be measured with NIR spectroscopy. In this redshift range, we utilize the GNIRS-DQS catalog in Paper I. GNIRS-DQS is the largest and most comprehensive inventory of rest-frame optical properties for luminous quasars, notably the $H\beta$, [O III], and Fe II emission lines. To complement this sample of high-redshift, high-luminosity quasars, we include an archival sample of quasars in the low-redshift regime from the BL04 subsample also utilized in SL15. In this redshift range ($z < 0.5$), the $H\beta$ emission properties can be obtained from optical spectra, but the C IV emission-line

properties are more difficult to obtain, and are available primarily from the *Hubble Space Telescope* (HST) and the *International Ultraviolet Explorer* (IUE) archives. Below, we briefly discuss the selection process for our ordinary quasar sample.

The GNIRS-DQS sources were selected to lie in three narrow redshift intervals, $1.55 \lesssim z \lesssim 1.65$, $2.10 \lesssim z \lesssim 2.40$, and $3.20 \lesssim z \lesssim 3.50$ to center the $H\beta + [\text{O III}]$ spectral complex in the NIR bands covered by GNIRS (i.e., the *J*, *H*, and *K* bands, respectively). In total, the survey comprises 260 sources with high-quality NIR spectra and comprehensive $H\beta$, $[\text{O III}]$, and Fe II spectral measurements (see [Matthews et al. 2021](#), and Paper I for more details). We exclude 64 BAL quasars, 16 radio-loud quasars (RLQs), and one quasar, SDSS J114705.24+083900.6 that is both BAL and radio loud. We define RLQs as sources having radio-loudness values of $R > 100$ (where R is the ratio between the flux densities at 5 GHz and 4400 Å; [Kellermann et al. 1989](#)). RLQs and BAL quasars are excluded to minimize the potential effects of continuum boosting from a jet (e.g., [Meusinger & Balafkan 2014](#)) and absorption biases (e.g., see BL04), respectively. Two quasars, SDSS J073132.18+461347.0 and SDSS J141617.38+264906.1, are excluded due to a lack of C IV measurements from Paper II. In total, 177 GNIRS-DQS quasars are included in our analysis; of these, seven sources with $\text{EW}(\text{C IV}) < 10 \text{ \AA}$ can be formally classified as WLQs (see Section 2.1). We adopt values of $\text{FWHM}(H\beta)$, $\nu L_\nu(5100 \text{ \AA})$, $\text{EW}(H\beta)$, and $\text{EW}(\text{Fe II})$ values from Paper I. The latter two parameters are used to derive $R_{\text{Fe II}}$. Paper II reports the $\text{EW}(\text{C IV})$ values and the wavelengths of the C IV emission-line peaks for the quasars in Paper I, which are then used to derive the Blueshift(C IV) values (see Section 2.3).

Sixty quasars at $z < 0.5$ from BL04 are added to our analysis from the 63 BL04 quasars in SL15. PG 0049+171, PG 1427+480, and PG 1415+451 are excluded due to a lack of published Fe II spectral measurements. The UV data in the BL04 sample comes, roughly equally, from both the *HST* and the *IUE* archives (see, [Baskin & Laor 2005](#)). Throughout this work, we check whether including only *HST* or *IUE* data changes the conclusion of the paper, but we find no statistical difference in the results of Section 3. Therefore, we include both subsets in this work. We obtain the $\text{FWHM}(H\beta)$, $\nu L_\nu(5100 \text{ \AA})$, and $R_{\text{Fe II}}$ values for the BL04 sources from [Boroson & Green \(1992\)](#), and their $\text{EW}(\text{C IV})$ and Blueshift(C IV) values from [Baskin & Laor \(2005\)](#). The line measurements are expected to be roughly consistent across the different samples utilized in this work, since they all employed similar standard fitting procedures.

Table 2 lists the basic properties of the ordinary quasars in our sample with the same formatting as Table 1.

2.3. Systemic redshifts and the Blueshift(C IV)

We derive the Blueshift(C IV) values of GNIRS-DQS sources from the observed wavelengths of the C IV emission-line peaks reported in Paper II and the systemic redshifts reported in Paper I. The Blueshift(C IV) values are derived following Equation (2) in [Dix et al. \(2020\)](#)

$$\frac{\Delta v}{\text{km s}^{-1}} = \left[\frac{c}{\text{km s}^{-1}} \right] \left(\frac{z_{\text{meas}} - z_{\text{sys}}}{1 + z_{\text{sys}}} \right), \quad (1)$$

where z_{meas} is the redshift measured from the wavelength of the C IV emission-line peak, and z_{sys} is the systemic redshift with respect to the $[\text{O III}]$, the Mg II , or the $H\beta$ emission lines reported in Paper I. In this work, we report the Blueshift(C IV) $\equiv -\Delta v$ values.

A non-negligible fraction ($\sim 1/3$) of luminous quasars have extremely weak or undetectable $[\text{O III}]$ emission (e.g., [Netzer et al. 2004](#)), so we must use alternative emission lines as the reference for z_{sys} (as was done for many ordinary GNIRS-DQS sources; see, Paper I). In spite of the larger intrinsic uncertainties associated with using the Mg II and $H\beta$ emission lines as z_{sys} indicators ($\sim 200 \text{ km s}^{-1}$ and $\sim 400 \text{ km s}^{-1}$, respectively; [Shen et al. 2016](#)), these uncertainties are typically much smaller than the Blueshift(C IV) values observed in the majority of luminous high-redshift quasars (see, Paper I). Therefore, the lack of $[\text{O III}]$ -based z_{sys} values for such sources should not affect the conclusions of this work significantly.

2.4. M_{BH} and L/L_{Edd} Estimates

Traditional estimation of single-epoch M_{BH} values has made use of the reverberation-mapping (RM) scaling relationship between the size of the $H\beta$ -emitting region ($R_{H\beta}$) and $\nu L_\nu(5100 \text{ \AA})$ (e.g., [Laor 1998](#); [Wandel et al. 1999](#); [Kaspi et al. 2005](#); [Bentz et al. 2013](#)). In this work, we use the empirical scaling relation established by [Bentz et al. \(2013\)](#) for consistency with other recent studies (e.g., [Maithil et al. 2022](#), Paper II):

$$\log \left[\frac{R_{H\beta}}{\text{lt} - \text{days}} \right] = (1.527 \pm 0.031) + (0.533 \pm 0.035) \log \ell_{44} \quad (2)$$

where $\ell_{44} \equiv \nu L_\nu(5100 \text{ \AA}) / 10^{44} \text{ erg s}^{-1}$.

Table 1. Basic Properties of the WLQ Sample

| Quasar | z_{sys} | $\log \nu L_{\nu}(5100 \text{ \AA})$ | FWHM(H β) | $R_{\text{Fe II}}$ | $\log M_{\text{BH}}$ | $\log M_{\text{BH, corr}}$ | L/L_{Edd} | $L/L_{\text{Edd, corr}}$ | EW(CIV) | Blueshift(CIV) | Optical | CIV |
|--------------------------|------------------|--------------------------------------|------------------|--------------------|----------------------|----------------------------|--------------------|--------------------------|---------------------|------------------------|----------|----------|
| (1) | (2) | (3) | (4) | (5) | (6) | (7) | (8) | (9) | (10) | (11) | (12) | (13) |
| | | (erg s $^{-1}$) | (km s $^{-1}$) | | (M_{\odot}) | (M_{\odot}) | | | (\AA) | (km s $^{-1}$) | Ref. a | Ref. a |
| SDSS J010643.23-031536.4 | 2.248 | 46.51 | 6782 | 0.58 | 9.99 | 9.71 | 0.20 | 0.39 | $7.6^{+0.6}_{-0.9}$ | 1451^{+119}_{-110} | 1 | 2 |
| SDSS J013136.44+130331.0 | 1.599 | 46.45 | 2294 | 0.78 | 9.02 | 8.67 | 1.63 | 3.67 | $2.8^{+1.4}_{-2.0}$ | 2320^{+521}_{-521} | 1 | 2 |
| SDSS J013417.81-005036.2 | 2.270 | 46.45 | 5211 | 0.98 | 9.73 | 9.31 | 0.32 | 0.84 | $7.3^{+0.7}_{-1.0}$ | 2233^{+651}_{-414} | 1 | 2 |
| SDSS J075115.43+505439.1 | 2.311 | 46.59 | 3077 | 3.05 | 9.35 | 8.19 | 1.05 | 15.04 | $6.6^{+0.6}_{-1.0}$ | 5953^{+234}_{-117} | 1 | 2 |
| SDSS J083650.86+142539.0 | 1.749 | 45.93 | 2880 | 2.48 | 8.94 | 8.04 | 0.62 | 4.95 | $4.2^{+0.3}_{-0.5}$ | 2266 ± 191 | 3 | 3 |
| SDSS J085337.36+121800.3 | 2.197 | 46.56 | 4502 | 0.28 | 9.66 | 9.48 | 0.47 | 0.73 | $7.7^{+1.1}_{-1.7}$ | 1166^{+363}_{-242} | 1 | 2 |
| SDSS J085344.17+354104.5 | 2.183 | 46.40 | 4168 | 0.72 | 9.51 | 9.18 | 0.47 | 1.00 | $4.3^{+0.8}_{-1.2}$ | 2053^{+1580}_{-1094} | 1 | 2 |
| SDSS J094533.98+100950.1 | 1.683 | 46.17 | 4278 | 2.00 | 9.41 | 8.66 | 0.35 | 2.03 | $2.9^{+0.3}_{-0.6}$ | 5485 ± 980 | 3 | 3 |
| SDSS J094602.31+274407.0 | 2.488 | 46.75 | 3833 | 1.65 | 9.63 | 8.94 | 0.79 | 3.82 | $5.9^{+0.4}_{-0.6}$ | 9062^{+16}_{-11} | 1 | 2 |
| SDSS J113747.64+391941.5 | 2.428 | 45.81 | 2518 | 3.31 | 8.76 | 7.57 | 0.72 | 10.99 | 8^{+6}_{-9} | 3089^{+2050}_{-1236} | 4 | 4 |
| SDSS J114153.33+021924.4 | 3.550 | 46.55 | 5900 | 3.25 | 9.89 | 8.67 | 0.27 | 4.60 | 0.4^{+2}_{-4} | -577^{+2461}_{-1484} | 5 | 6,4 |
| SDSS J123743.07+630144.7 | 3.490 | 46.35 | 5200 | 2.86 | 9.68 | 8.61 | 0.29 | 3.39 | 1 ± 2 | -970^{+1349}_{-876} | 5 | 4 |
| SDSS J141141.96+140233.9 | 1.754 | 45.64 | 3966 | 1.41 | 9.06 | 8.56 | 0.24 | 0.78 | $3.8^{+0.8}_{-0.2}$ | 3142^{+378}_{-208} | 1 | 2 |
| SDSS J141730.92+073320.7 | 1.716 | 45.91 | 2784 | 1.65 | 8.90 | 8.29 | 0.65 | 2.64 | $2.5^{+2.1}_{-0.7}$ | 5321^{+4178}_{-872} | 1 | 2 |
| SDSS J144741.76-020339.1 | 1.430 | 45.56 | 1923 | 1.60 | 8.39 | 7.83 | 0.96 | 3.52 | $7.7^{+0.2}_{-1.3}$ | 1319^{+759}_{-381} | 1 | 2 |
| SDSS J152156.48+520238.5 | 2.190 | 47.14 | 5750 | 1.64 | 10.19 | 9.48 | 0.52 | 2.69 | 9.1 ± 0.6 | 4900 ± 300 | 7 | 7 |
| SDSS J213742.25-003912.7 | 2.294 | 45.75 | 2630 | 2.45 | 8.77 | 7.89 | 0.62 | 4.68 | 3^{+1}_{-2} | 4986^{+867}_{-535} | 4 | 4 |
| PHL 1811 | 0.192 | 45.56 | 1943 | 1.29 ^C | 8.40 | 7.94 | 0.94 | 2.70 | 6.6 | 1400 ± 250 | 8 | 8 |

^a Source of rest-frame optical-UV data, Column (12); z_{sys} , $\nu L_{\nu}(5100 \text{ \AA})$, FWHM(H β), $R_{\text{Fe II}}$, Column (13); EW(CIV), and Blueshift(CIV). (1) Paper I; (2) Paper II; (3) Plotkin et al. (2015); (4) this work; (5) Shemmer et al. (2010); (6) Shen et al. (2011); (7) Wu et al. (2011); (8) Leighly et al. (2007).

^b Wu et al. (2011) also reported H β -based Blueshift(CIV) = 9400 km s $^{-1}$. Here, we have opted to use a Mg II-based value of Blueshift(CIV).

^c Leighly et al. (2007) reported the $R_{\text{Fe II}}$ value as being in the range 1.22-1.35. We have adopted a mean value of 1.29 for this work.

Table 2. Basic Properties of the Ordinary Quasar Sample

| Quasar | z_{sys} | $\log \nu L_{\nu}(5100 \text{ \AA})$ (erg s^{-1}) | FWHM(H β) (km s^{-1}) | $R_{\text{Fe II}}$ | $\log M_{\text{BH}}$ (M_{\odot}) | $\log M_{\text{BH, corr}}$ (M_{\odot}) | L/L_{Edd} | $L/L_{\text{Edd, corr}}$ | EW(C IV) (\AA) | Blueshift(C IV) (km s^{-1}) | Optical Ref. ^a | C IV Ref. ^a |
|--------------------------|------------------|---|--|--------------------|---|---|--------------------|--------------------------|---|---|------------------------------|---------------------------|
| (1) | (2) | (3) | (4) | (5) | (6) | (7) | (8) | (9) | (10) | (11) | (12) | (13) |
| PG 0003+199 | 0.026 | 44.07 | 1640 | 0.62 | 7.46 | 7.36 | 0.33 | 0.41 | 60.1 ^b | -102 | 3 | 4 |
| SDSS J001018.88+280932.5 | 1.613 | 46.27 | 3189 | 0.06 | 9.21 | 9.13 | 0.70 | 0.86 | 61.0 ^{+0.5} _{-0.8} | 203 ⁺²² ₋₁₅ | 1 | 2 |
| SDSS J001453.20+091217.6 | 2.335 | 46.36 | 6428 | 0.72 | 9.87 | 9.54 | 0.19 | 0.40 | 39.0 ^{+3.3} _{-5.0} | 825 ⁺³⁹⁷ ₋₂₆₆ | 1 | 2 |
| SDSS J001813.30+361058.6 | 2.333 | 46.46 | 4896 | 0.55 | 9.68 | 9.41 | 0.36 | 0.68 | 25.8 ^{+1.1} _{-1.6} | 2689 ⁺²⁰³ ₋₁₃₆ | 1 | 2 |
| SDSS J001914.46+155555.9 | 2.267 | 46.34 | 4033 | 0.17 | 9.45 | 9.32 | 0.47 | 0.64 | 44.5 ^{+0.9} _{-1.3} | 372 ⁺¹¹⁰ ₋₇₄ | 1 | 2 |
| PG 0026+129 | 0.145 | 45.13 | 1860 | 0.51 | 8.13 | 7.98 | 0.68 | 0.95 | 19.3 | -120 | 3 | 4 |
| SDSS J002634.46+274015.5 | 2.247 | 46.38 | 4420 | 0.00 | 9.55 | 9.48 | 0.41 | 0.49 | 134.6 ^{+10.1} _{-15.0} | 400 ⁺⁴¹⁶ ₋₂₇₉ | 1 | 2 |
| SDSS J003001.11-015743.5 | 1.590 | 46.10 | 4028 | 0.26 | 9.32 | 9.18 | 0.37 | 0.52 | 52.7 ^{+1.9} _{-2.8} | 1279 ⁺¹³⁹ ₋₉₃ | 1 | 2 |
| SDSS J003416.61+002241.1 | 1.631 | 46.24 | 5527 | 0.44 | 9.67 | 9.46 | 0.23 | 0.38 | 28.5 ^{+0.3} _{-0.5} | 597 ⁺⁸⁶ ₋₅₈ | 1 | 2 |
| SDSS J003853.15+333044.3 | 2.373 | 46.39 | 4297 | 0.50 | 9.53 | 9.28 | 0.44 | 0.78 | 13.8 ^{+1.0} _{-1.5} | 670 ⁺⁹⁴⁷ ₋₆₃₅ | 1 | 2 |

^a Source of rest-frame optical-UV data, Column (12): $z_{\text{sys}}, \nu L_{\nu}(5100 \text{ \AA}), \text{FWHM}(\text{H}\beta), R_{\text{Fe II}}$; Column (13): EW(C IV), and Blueshift(C IV). (1) Paper I; (2) Paper II; (3) Boroson & Green (1992); (4) Baskin & Laor (2005).

^b There are no errors reported for EW(C IV) and Blueshift(C IV) values for PG quasars in Baskin & Laor (2005).

NOTE—Only the first ten lines are shown; the entire table is available in the electronic version.

However, the $H\beta$ RM sample was subsequently determined to be biased toward objects with strong, narrow [O III] emission-lines, and, in effect, is biased in favor of low-accretion-rate broad-line AGNs (see, e.g., Robinson 1994; Shen & Ho 2014). Recent RM campaigns aimed at minimizing such bias, such as the Super-Eddington Accreting Massive Black Hole (SEAMBH; Du et al. 2014; 2016; 2018) and the SDSS-RM project (Shen et al. 2015), found deviations from the traditional size-luminosity relationship. In particular, SEAMBH found a population of rapidly accreting AGNs with a BELR size up to 3-8 times smaller than predicted by Equation 2, which implies an overestimation of super-Eddington-accreting M_{BH} values from single-epoch spectra by the same factor. We apply a $R_{\text{Fe II}}$ correction to the traditional $H\beta$ -based M_{BH} estimation, a method developed by Du & Wang (2019). The $R_{\text{Fe II}}$ parameter has been shown to correlate with L/L_{Edd} (e.g., Netzer & Trakhtenbrot 2007).

For the Fe II-corrected values of M_{BH} (hereafter, $M_{\text{BH, corr}}$), we apply the size-luminosity scaling relation for $R_{H\beta}$ following Equation (5) of Du & Wang (2019):

$$\begin{aligned} & \log \left[\frac{R_{H\beta, \text{corr}}}{\text{lt-days}} \right] \\ &= (1.65 \pm 0.06) + (0.45 \pm 0.03) \log \ell_{44} \\ &+ (-0.35 \pm 0.08) R_{\text{Fe II}}. \end{aligned} \quad (3)$$

Subsequently, $M_{\text{BH}} (M_{\text{BH, corr}})$ can be estimated using the following relationship:

$$\begin{aligned} & \frac{M_{\text{BH}} (M_{\text{BH, corr}})}{M_{\odot}} \\ &= f \left[\frac{R_{\text{BELR}}}{\text{pc}} \right] \left[\frac{\Delta V}{\text{km s}^{-1}} \right]^2 \left[\frac{G}{\text{pc } M_{\odot}^{-1} (\text{km s}^{-1})^2} \right]^{-1} \\ &\approx 1.5 \left[\frac{R_{H\beta} (R_{H\beta, \text{corr}})}{\text{pc}} \right] \left[\frac{\text{FWHM}(H\beta)}{\text{km s}^{-1}} \right]^2 \\ &\cdot \left[\frac{4.3 \times 10^{-3}}{\text{pc } M_{\odot}^{-1} (\text{km s}^{-1})^2} \right]^{-1}, \end{aligned} \quad (4)$$

where we adopt $f = 1.5$ for the virial coefficient, consistent with results from Ho & Kim (2014); Yu et al. (2019, 2020a); Maithil et al. (2022), $R_{\text{BELR}} \approx R_{H\beta}$ ($R_{H\beta, \text{corr}}$) is the size-luminosity relation from Equation 2 (3), ΔV is the velocity width of the emission line, which is taken here as $\text{FWHM}(H\beta)$, assuming Doppler broadening (Wandel et al. 1999), and G is the gravitational constant.

The L/L_{Edd} parameter can be computed from the corresponding M_{BH} value following Equation (2) of Shem-

mer et al. (2010) assuming that L_{Edd} is computed for the case of solar metallicity:

$$\begin{aligned} & L/L_{\text{Edd}} (L/L_{\text{Edd, corr}}) \\ &= 1.06 f(L) \left[\frac{\nu L_{\nu}(5100 \text{ \AA})}{10^{44} \text{ ergs s}^{-1}} \right] \left[\frac{M_{\text{BH}} (M_{\text{BH, corr}})}{10^6 M_{\odot}} \right]^{-1}, \end{aligned} \quad (5)$$

where $f(L)$ is the luminosity-dependent bolometric correction to $\nu L_{\nu}(5100 \text{ \AA})$, derived from Equation (21) of Marconi et al. (2004).

We note that a wide range of bolometric corrections for quasars is available in the literature (e.g., Richards et al. 2006; Nemmen & Brotherton 2010; Runnoe et al. 2012; Netzer 2019). However, in general, the range of these corrections is not large enough to affect the conclusion of our work. For example, Maithil et al. (2022) recently used a constant bolometric correction of $L_{\text{Bol}}/\nu L_{\nu}(5100 \text{ \AA}) \sim 9$; the bolometric corrections we derive are in the range of ~ 5 -6, which results in a relatively small *systematic* offset in the derivation of the L/L_{Edd} parameter.

The uncertainties associated with the corrected M_{BH} and L/L_{Edd} values in this work are estimated to be at least ~ 0.3 dex (see Table 2 of Maithil et al. 2022), but could be much larger ($\sim 0.4 - 0.6$ dex) for high L/L_{Edd} objects such as WLQs (see also, SL15).

3. RESULTS AND DISCUSSION

3.1. Black Hole Masses and Accretion Rates

For the 248 quasars included in this work, we determine the virial $H\beta$ -based $M_{\text{BH, corr}}$ and corresponding $L/L_{\text{Edd, corr}}$ values from their derived optical properties, following the Fe II-corrected BELR size-luminosity relation of Equation 3, applied to Equations 4 and 5. We also calculate these quasars' M_{BH} and L/L_{Edd} values following the traditional BELR size-luminosity relation of Equation 2 to compare the two methods for estimating black-hole masses and accretion rates.

Figure 1 presents the traditional versus corrected M_{BH} and L/L_{Edd} values for the quasars in our sample, following the procedure of Maithil et al. (2022). The $H\beta$ -based $M_{\text{BH, corr}}$ values of ordinary quasars show small systematic deviations from the traditional BELR size-luminosity relation estimates (less than a factor of two for 222 out of 230 quasars). On the other hand, for a majority of the WLQs, due to the relative weakness in $H\beta$ emission compared to the Fe II emission, $M_{\text{BH, corr}}$ values deviate significantly from the traditional relation, by up to one order of magnitude. Since L/L_{Edd} is inversely proportional to M_{BH} , the $L/L_{\text{Edd, corr}}$ values are enhanced by a similar factor.

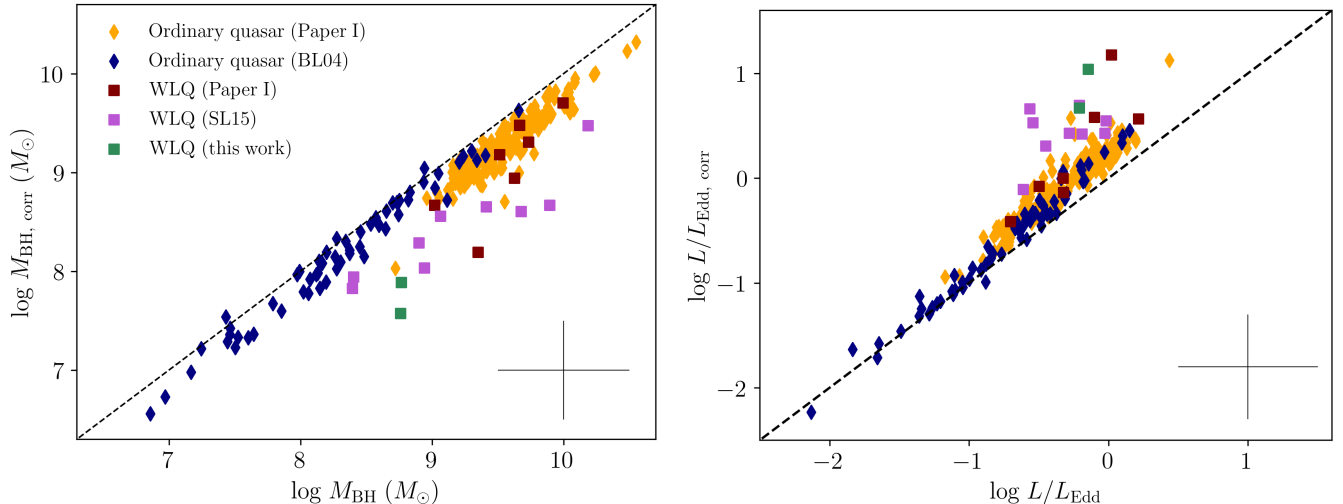


Figure 1. Black-hole mass (left panel) and accretion rate (right panel) calculated using the traditional (x-axis) and $R_{\text{Fe II}}$ -corrected (y-axis) BELR size-luminosity relation for all quasars in our analysis. Diamonds mark ordinary quasars and squares mark WLQs. The dashed lines represent a one-to-one relation between the two methods. Typical uncertainties of 0.5 dex on the M_{BH} and L/L_{Edd} values are displayed in the bottom right corner of each panel. The traditional relation overestimates M_{BH} in rapidly-accreting quasars by up to an order of magnitude. In turn, the traditional relation underestimates L/L_{Edd} by a similar factor. In particular, the $R_{\text{Fe II}}$ -corrected accretion rates are much larger for a considerably larger fraction of sources in the WLQ subset than in the ordinary quasars, due to their larger $R_{\text{Fe II}}$ values.

This result is in line with the Maithil et al. (2022) finding of a larger deviation from the one-to-one relation in high-accretion-rate quasars.

3.2. The Anti-correlation between $\text{EW}(\text{C IV})$ and L/L_{Edd}

We use our sample to explore the anti-correlation between $\text{EW}(\text{C IV})$ and $\text{H}\beta$ -based L/L_{Edd} previously studied in SL15 (i.e., the MBE), as well as with $L/L_{\text{Edd, corr}}$. Figure 2 shows $\text{EW}(\text{C IV})$ plotted against the traditional L/L_{Edd} values (left) and against the Fe II-corrected $L/L_{\text{Edd, corr}}$ values (right). The first four rows of Table 3 present the respective Spearman-rank correlation coefficients (r_S) and chance probabilities (p) of the ordinary quasar sample and the complete sample, including WLQs, for the correlation involving $\text{EW}(\text{C IV})$. We detect significant anti-correlations between $\text{EW}(\text{C IV})$ and L/L_{Edd} both with and without WLQs (i.e., $p \ll 1\%$). However, the anti-correlation for the sample including WLQs is slightly weaker than without WLQs (both p values are roughly similar, but r_S increases slightly). Our result reaffirms findings by SL15, who found WLQs to be outliers in this relation.

With a Fe II correction, the $L/L_{\text{Edd, corr}}$ values provide a significantly stronger anti-correlation with $\text{EW}(\text{C IV})$ as the r_S value decreases from -0.36 (for the L/L_{Edd} case) to -0.48 . Furthermore, the inclusion of WLQs no longer spoils the Spearman-rank correlation; in fact, the p value remains extremely low ($p = 4.02 \times 10^{-20}$ for the entire sample), and the r_S value

decreases from -0.48 to -0.54 , indicative of a stronger anti-correlation. Nevertheless, the $L/L_{\text{Edd, corr}}$ values of most of the WLQs in our sample still appear considerably smaller than a linear model would suggest (see Figure 2). To quantify the deviation of WLQs from the MBE, we fit a simple linear model, without considering the errors, to the $\log \text{EW}(\text{C IV})$ and $\log L/L_{\text{Edd, corr}}$ values of the ordinary quasar sample. Our WLQs deviate from the best-fit model by a mean of $\sim 3.4\sigma$, with a range in deviation from 1.08σ to 8.02σ . Such a discrepancy paints WLQs as significant outliers in this correlation.

We also explore whether a bolometric luminosity correction based on the peculiarity of WLQs could account for this discrepancy. Although several methods for correcting bolometric luminosity are available in the literature (e.g., Richards et al. 2006; Nemmen & Brotherton 2010; Runnoe et al. 2012; Netzer 2019), if the Eddington ratios of WLQs were to be reliably predicted by the MBE, these corrections must be up to $\sim 10^5$ times larger than those of Marconi et al. (2004) (as in the case of SDSS J1141+0219 with $\text{EW}(\text{C IV}) = 0.4 \text{ \AA}$). Such a discrepancy is larger than the difference expected by any of the current bolometric correction methods in the literature. These results reveal that $\text{EW}(\text{C IV})$ is likely not the sole indicator of accretion rate in all quasars, in agreement with SL15.

3.3. The C IV || Distance as an Indicator of L/L_{Edd}

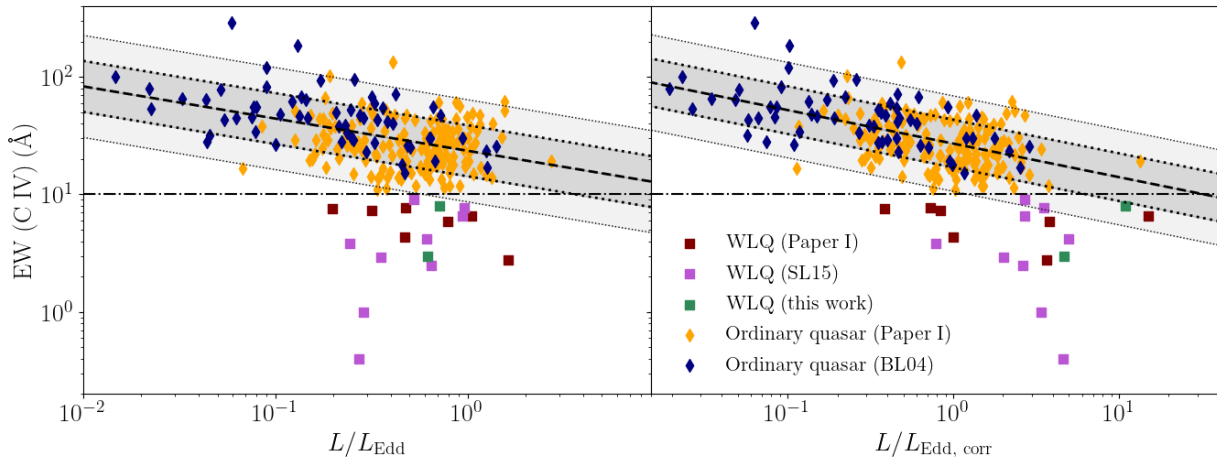


Figure 2. Correlation between $\text{EW}(\text{C IV})$ and L/L_{Edd} of ordinary quasars (diamonds) and WLQs from Table 1 (squares). The left panel presents the traditional L/L_{Edd} values, and the right panel displays the Fe II-corrected $L/L_{\text{Edd, corr}}$ values. The dotted-dashed lines represent the EW threshold below which objects are defined as WLQs. The correlation for the ordinary quasar sample, obtained by fitting a linear model, is shown as a dashed line. The shaded regions represent the 1- and 2- σ deviations from the fitted correlation. Correcting the traditional L/L_{Edd} values results in a stronger anti-correlation expected by the MBE (see Table 3); however, WLQs’ $L/L_{\text{Edd, corr}}$ values are still considerably (more than an order of magnitude) over-predicted by the MBE, suggesting that $\text{EW}(\text{C IV})$ is not the sole indicator of quasars’ accretion rates.

Rivera et al. (2020) used an independent component analysis (ICA) technique to analyze the spectral properties of the C IV emission line in 133 quasars from the SDSS-RM project (Shen et al. 2015). In particular, they fitted a piece-wise polynomial to trace the positions of these sources on the $\text{EW}(\text{C IV})$ and the Blueshift(C IV) plane. The projected position of a quasar along this curve is defined as its ‘C IV || Distance’. To calculate the value of this C IV || Distance parameter, we follow the procedure summarized in R22 and detailed in McCaffrey & Richards (2021). In short, we first transform the values of the two axes ($\text{EW}(\text{C IV})$ and Blueshift(C IV)) to lie between 0 and 1, using the `MinMaxScaler` function within `scikit-learn` (Pedregosa et al. 2011). Then, the C IV || Distance values are measured relative to the first point of the best-fit curve, located at $\text{EW}(\text{C IV}) \approx 316 \text{ \AA}$ and Blueshift(C IV) $\approx 50 \text{ km s}^{-1}$. This parameter essentially indicates the location along a non-linear first principal component of the C IV parameter space, and encodes information about the physics of the C IV-emitting gas (e.g., Richards et al. 2011, 2021; Giustini & Proga 2019).

The left panel of Figure 3 shows the distribution of $\text{EW}(\text{C IV})$ versus Blueshift(C IV) of the 248 quasars in our sample. The right panel of Figure 3 shows the same distribution in scaled space, following the procedure in McCaffrey & Richards (2021), and the piece-wise polynomial best-fit curve from Figure 2 of R22. Even though our sources are drawn from samples that are different from those of R22, the best-fit curve traces the C IV parameter space of sources across wide ranges of redshifts

and luminosities. Since all quasars in our sample are selected photometrically, either in optical (for GNIRS-DQS quasars) or UV (for BL04 quasars) surveys, and were not selected based on their spectroscopic characteristics, there are no known biases associated with their selection, and thus they are expected to trace the C IV parameter space in a similar manner to larger samples of quasars in other studies (e.g., see also Rankine et al. 2020).

While the $\text{EW}(\text{C IV})$ parameter, on its own, is not an ideal accretion-rate indicator, the C IV || Distance parameter appears to provide a robust indication of the accretion rates for all quasars including WLQs. We plot the C IV || Distance versus $H\beta$ -based L/L_{Edd} (left) and $L/L_{\text{Edd, corr}}$ (right) for all quasars in our sample in Figure 4. The last four rows of Table 3 provide the Spearman-rank correlation coefficients and chance probabilities for the correlations involving the C IV || Distance. Both the L/L_{Edd} and $L/L_{\text{Edd, corr}}$ are significantly correlated with the C IV || Distance parameter (i.e., $p \ll 1\%$).

In the case of C IV || Distance versus $L/L_{\text{Edd, corr}}$, the correlation coefficient is considerably larger than the correlation involving L/L_{Edd} (0.57 versus 0.36), indicating the importance of the Fe II correction to M_{BH} . Furthermore, the inclusion of WLQs in the sample both strengthens the correlation (r_S increases from 0.52 to 0.57 while the p value remains extremely small, $< 10^{-16}$), and allows the high- $L/L_{\text{Edd, corr}}$ end of the correlation to be more populated. There is also no significant deviation of the WLQs from this correlation,

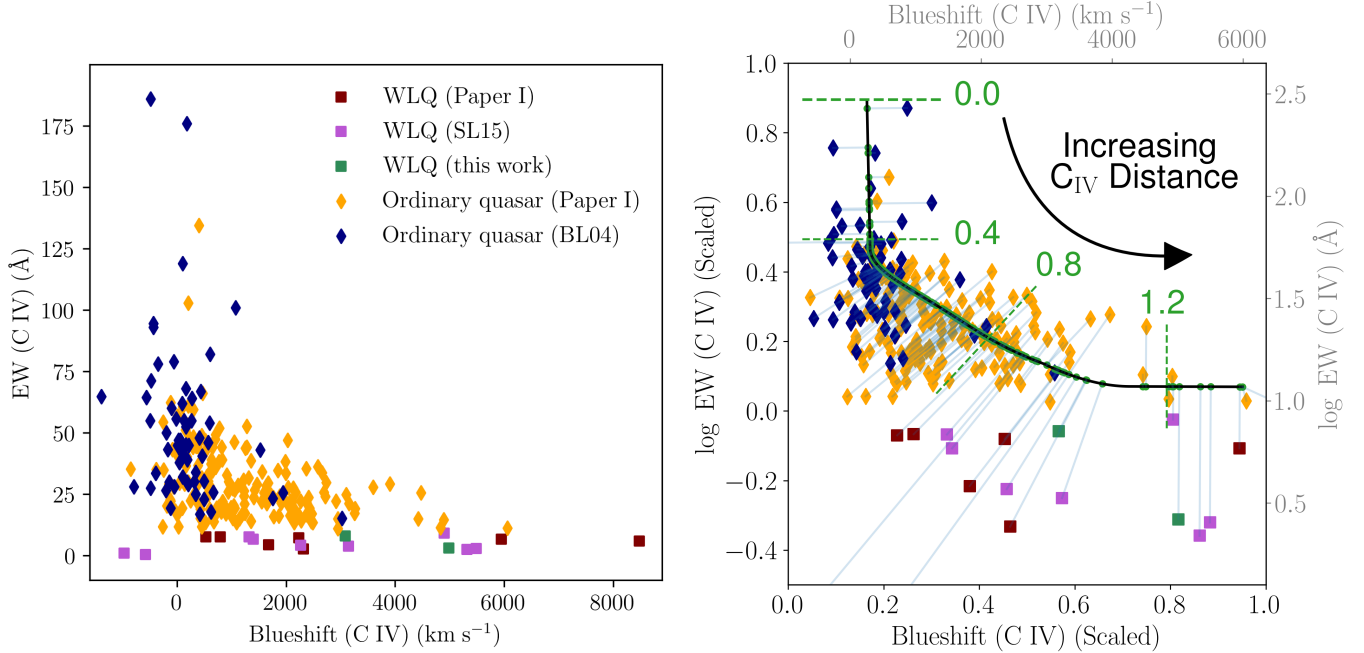


Figure 3. Left panel: distribution of EW(C IV) versus Blueshift(C IV) for our sample. One quasar from BL04, PG 1202+281, is not shown in the left panel, due to its extremely high EW(C IV) = 290 Å. Right panel: illustration of the C IV || Distance parameter. The data are first scaled so that the two axes share the same limit, then each data point is projected onto the best-fit curve obtained from R22. The C IV || Distance value of each quasar is defined as its projected position (green point) along the solid black curve. Three of the WLQs, SDSS J114153.33+021924.4, SDSS J123743.07+630144.7, SDSS J094602.31+274407.0, and one ordinary quasar, PG 1202+281, are not shown in the right panel, for clarity, but only their projected positions onto the curve are relevant to our results.

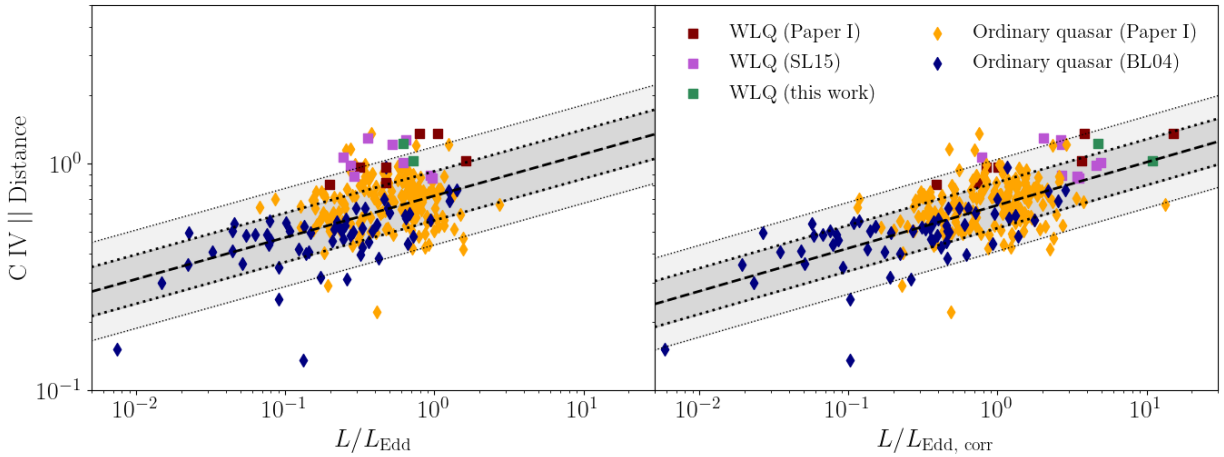


Figure 4. C IV || Distance versus L/L_{Edd} of 248 quasars in our sample. In the left panel, the C IV || Distance values are plotted against the traditional H β -based L/L_{Edd} parameter, and in the right panel, against the Fe II-corrected H β -based $L/L_{\text{Edd,corr}}$ parameter. The ordinary quasar PG 1202+281 with $L/L_{\text{Edd,corr}} = 0.06$ and C IV || Distance = 0.02 is not plotted, for clarity. The correlation for the ordinary quasar sample, obtained by fitting a linear model, is shown as a dashed line. The shaded regions represent the 1- and 2- σ deviations from the fitted correlation. While using the traditional size-luminosity relation to estimate accretion rates already yields a strong correlation, the Fe II-corrected accretion rates show a much stronger correlation with the C IV || Distance parameter for *all* quasars. Furthermore, this parameter serves as a better predictor for $L/L_{\text{Edd,corr}}$ than for L/L_{Edd} .

as opposed to their behavior in the MBE (see, Figure 2) as well as in the C IV || Distance versus traditional L/L_{Edd} (see left panel of Figure 4). To quantify this effect, we fit a linear model to the C IV || Distance and L/L_{Edd} ($L/L_{\text{Edd, corr}}$) space, taking into account only the ordinary quasars. Then, we calculate the mean scatter of the WLQs from this line. In the case of L/L_{Edd} , we find the deviation from the best-fit line to range from 0.62σ to 2.96σ , and the mean deviation to be $\sim 1.8\sigma$. Meanwhile, the deviation in the case of $L/L_{\text{Edd, corr}}$ ranges from 0.01σ to 2.18σ , with a mean deviation of $\sim 1.1\sigma$. Thus, using $L/L_{\text{Edd, corr}}$ not only results in a stronger correlation with C IV || Distance, but C IV || Distance also serves as a better predictor for $L/L_{\text{Edd, corr}}$ than for L/L_{Edd} .

The right panel of Figure 4 shows that WLQs are not a disjoint subset of quasars in the UV–optical space (see also, Martínez-Aldama et al. 2018). Our results indicate that WLQs possess relatively high accretion rates, due not only to their extremely weak C IV lines, but rather to their relatively large values of the C IV || Distance parameter. Similarly, we observe quasars with high accretion rates (and large values of C IV || Distance) that do not necessarily possess extremely weak C IV lines, some of which have Eddington ratios that are larger than those of several WLQs. Finally, while we are unaware of a large population of quasars that deviate significantly from the correlations of Figure 4, a future examination of, e.g., H β -based L/L_{Edd} values of quasars with very large EW(C IV) (e.g., Fu et al. 2022) is warranted to further test our results.

In this work, we show that the C IV and H β parameter space provides important diagnostics for quasar physics. In particular, we found that the C IV || Distance can serve as a robust predictor of quasar’s accretion rate, especially after a correction based on $R_{\text{Fe II}}$ is applied. Within the limits of our sample, we also find that WLQs are not a disjoint subset of the Type 1 quasar population, but instead lie preferentially toward the extreme end of the C IV–H β parameter space.

4. CONCLUSIONS

We compile a statistically meaningful sample of ordinary quasars and WLQs to study the dependence of quasar accretion rates, corrected for the relative strength of Fe II emission with respect to H β , upon source location in the C IV parameter space. Utilizing 18 WLQs, 16 of which are obtained from the literature and two of which are presented in this work, we confirm the findings of Maithil et al. (2022) that the tra-

ditional approach to estimating the Eddington ratio for rapidly-accreting quasars systematically underestimates this property by up to an order of magnitude compared to Fe II-corrected values of this parameter.

Using the Fe II-corrected values of H β -based L/L_{Edd} , we investigate the correlation between this parameter and the C IV parameter space. We confirm and strengthen the SL15 results by finding that WLQs spoil the anti-correlation between EW(C IV) and H β -based L/L_{Edd} for quasars, whether the latter parameter is estimated using the traditional method, or whether a correction based on Fe II emission is employed in the M_{BH} estimate. In keeping with SL15, we conclude that the EW(C IV) cannot be the sole indicator of accretion rate in quasars.

We also investigate the relationships between a recently-introduced parameter, the C IV || Distance, which is a combination of EW(C IV) and Blueshift(C IV), and the traditional H β -based L/L_{Edd} and the Fe II-corrected $L/L_{\text{Edd, corr}}$. Such relationships yield strong correlations, especially in the case of Fe II-corrected $L/L_{\text{Edd, corr}}$, and can accommodate *all* the quasars in our sample. Our finding suggests that WLQs are not a disjoint subset of sources from the general population of quasars. We find that many WLQs have extremely high accretion rates which is indicated by their preferentially higher values of the C IV || Distance parameter. Similarly, we find several quasars in our sample that possess high Eddington ratios, and correspondingly large values of the C IV || Distance, that do not have extremely weak C IV lines; some of these sources display Eddington ratios that are larger than those of a subset of our WLQs.

In the context of the C IV parameter space, it will be interesting to investigate whether the extreme X-ray properties of WLQs are the result of extremely large C IV || Distance values rather than resulting only from extremely weak C IV lines. Such a test would require X-ray coverage of a large sample of sources with H β +Fe II data across the widest possible C IV parameter space such as the GNIRS-DQS sample of Paper I. It would also be useful to determine whether the weakness of the broad Ly α +N V emission line complex (from which the first high-redshift WLQs were identified) also correlates with C IV || Distance, which will require rest-frame ultraviolet spectroscopy (Paul et al. 2022). The results of these investigations will shed new light on the connection between the quasar accretion rate and the physics of the inner accretion disk and BELR.

Table 3. Spearman-Rank Correlation Coefficients

| Correlation | Sample | N | r_s | p |
|--|----------|-----|-------|------------------------|
| EW(C IV)- L/L_{Edd} | Ordinary | 230 | -0.36 | 1.39×10^{-8} |
| EW(C IV)- L/L_{Edd} | All | 248 | -0.35 | 1.10×10^{-8} |
| EW(C IV)- $L/L_{\text{Edd, corr}}$ | Ordinary | 230 | -0.48 | 6.82×10^{-15} |
| EW(C IV)- $L/L_{\text{Edd, corr}}$ | All | 248 | -0.54 | 4.02×10^{-20} |
| C IV Distance- L/L_{Edd} | Ordinary | 230 | 0.37 | 6.50×10^{-9} |
| C IV Distance- L/L_{Edd} | All | 248 | 0.36 | 4.17×10^{-9} |
| C IV Distance- $L/L_{\text{Edd, corr}}$ | Ordinary | 230 | 0.52 | 3.16×10^{-17} |
| C IV Distance- $L/L_{\text{Edd, corr}}$ | All | 248 | 0.57 | 1.97×10^{-22} |

NOTE—The last three columns represent the number of sources in each correlation, the Spearman-rank correlation coefficient, and the chance probability, respectively.

Software: IRAF (Tody 1986), matplotlib (Hunter 2007), numpy (van der Walt et al. 2011; Harris et al. 2020), pandas (Wes McKinney 2010), scipy (Virtanen et al. 2020), scikit-learn (Pedregosa et al. 2011).

1 This work is supported by National Science Foundation
2 (NSF) grants AST-1815281 (B.M.M., O.S., C.D.), AST-
3 1815645 (M.S.B., A.D.M., J.M.). G.T.R. was supported
4 in part by NASA through a grant (HST-AR-15048.001-
5 A) from the Space Telescope Science Institute, which
6 is operated by the Association of Universities for Re-
7 search in Astronomy, Incorporated, under NASA con-
8 tract NAS5-26555. W.N.B. acknowledges support from
9 NSF grant AST-2106990. B.L. acknowledges financial
10 support from the National Natural Science Foundation
11 of China grant 11991053. B.T. acknowledges support
12 from the European Research Council (ERC) under the
13 European Union’s Horizon 2020 research and innova-
14 tion program (grant agreement 950533) and from the
15 Israel Science Foundation (grant 1849/19). We thank
16 an anonymous referee for the insightful comments and
17 suggestions which improved the clarity of this paper.
18 This research has made use of the NASA/IPAC Extra-
19 galactic Database (NED), which is operated by the Jet
20 Propulsion Laboratory, California Institute of Technol-
21 ogy, under contract with the National Aeronautics and
22 Space Administration.

REFERENCES

- Anderson, S. F., Fan, X., Richards, G. T., et al. 2001, *AJ*, 122, 503
- Bañados, E., Venemans, B. P., Decarli, R., et al. 2016, *ApJS*, 227, 11
- Baldwin, J. A. 1977, *ApJ*, 214, 679
- Baskin, A., & Laor, A. 2004, *MNRAS*, 350, L31
- . 2005, *MNRAS*, 356, 1029
- Bentz, M. C., Denney, K. D., Grier, C. J., et al. 2013, *ApJ*, 767, 149
- Boroson, T. A., & Green, R. F. 1992, *ApJS*, 80, 109
- Collinge, M. J., Strauss, M. A., Hall, P. B., et al. 2005, *AJ*, 129, 2542
- Diamond-Stanic, A. M., Fan, X., Brandt, W. N., et al. 2009, *ApJ*, 699, 782
- Dix, C., Shemmer, O., Brotherton, M. S., et al. 2020, *The Astrophysical Journal*, 893, 14
- Dix, C., Matthews, B., Shemmer, O., et al. 2023, arXiv preprint arXiv:2304.02142
- Dong, X.-B., Wang, T.-G., Wang, J.-G., et al. 2009, *ApJL*, 703, L1
- Du, P., & Wang, J.-M. 2019, *ApJ*, 886, 42

- Du, P., Wang, J.-M., Hu, C., et al. 2016, *ApJL*, 818, L14
- Du, P., Hu, C., Lu, K.-X., et al. 2014, *ApJ*, 782, 45
- Du, P., Zhang, Z.-X., Wang, K., et al. 2018, *ApJ*, 856, 6
- Fan, X., Strauss, M. A., Gunn, J. E., et al. 1999, *ApJL*, 526, L57
- Fu, S., Brandt, W. N., Zou, F., et al. 2022, *ApJ*, 934, 97
- Giustini, M., & Proga, D. 2019, *A&A*, 630, A94
- Harris, C. R., Millman, K. J., van der Walt, S. J., et al. 2020, *Nature*, 585, 357
- Ho, L. C., & Kim, M. 2014, *ApJ*, 789, 17
- Hryniewicz, K., Czerny, B., Nikolajuk, M., & Kuraszekiewicz, J. 2010, *MNRAS*, 404, 2028
- Hunter, J. D. 2007, *CSE*, 9, 90
- Jarrett, T. H., Cohen, M., Masci, F., et al. 2011, *ApJ*, 735, 112
- Just, D. W., Brandt, W. N., Shemmer, O., et al. 2007, *ApJ*, 665, 1004
- Kaspi, S., Maoz, D., Netzer, H., et al. 2005, *ApJ*, 629, 61
- Kellermann, K. I., Sramek, R., Schmidt, M., Shaffer, D. B., & Green, R. 1989, *AJ*, 98, 1195
- Lane, R. A., Shemmer, O., Diamond-Stanic, A. M., et al. 2011, *ApJ*, 743, 163
- Laor, A. 1998, *ApJL*, 505, L83
- Leighly, K. M., Halpern, J. P., Jenkins, E. B., & Casebeer, D. 2007, *ApJS*, 173, 1
- Luo, B., Brandt, W. N., Hall, P. B., et al. 2015, *ApJ*, 805, 122
- Lyke, B. W., Higley, A. N., McLane, J. N., et al. 2020, *ApJS*, 250, 8
- Maithil, J., Brotherton, M. S., Shemmer, O., et al. 2022, *MNRAS*
- Marconi, A., Risaliti, G., Gilli, R., et al. 2004, *MNRAS*, 351, 169
- Marlar, A., Shemmer, O., Anderson, S. F., et al. 2018, *ApJ*, 865, 92
- Martínez-Aldama, M. L., del Olmo, A., Marziani, P., et al. 2018, *A&A*, 618, A179
- Massaro, F., Marchesini, E. J., D'Abrusco, R., et al. 2017, *ApJ*, 834, 113
- Matthews, B. M., Dix, C., Shemmer, O., et al. 2023, under review
- Matthews, B. M., Shemmer, O., Dix, C., et al. 2021, *ApJS*, 252, 15
- McCaffrey, T. V., & Richards, Gordon T., C. 2021, doi: <https://doi.org/10.17918/CIVdistance>
- Meusinger, H., & Balafkan, N. 2014, *A&A*, 568, A114
- Nemmen, R. S., & Brotherton, M. S. 2010, *MNRAS*, 408, 1598
- Netzer, H. 2019, *MNRAS*, 488, 5185
- Netzer, H., Lira, P., Trakhtenbrot, B., Shemmer, O., & Cury, I. 2007, *The Astrophysical Journal*, 671, 1256
- Netzer, H., Shemmer, O., Maiolino, R., et al. 2004, *ApJ*, 614, 558
- Netzer, H., & Trakhtenbrot, B. 2007, *ApJ*, 654, 754
- Ni, Q., Brandt, W. N., Luo, B., et al. 2018, *MNRAS*, 480, 5184
- . 2022, *MNRAS*, 511, 5251
- Paul, J. D., Plotkin, R. M., Shemmer, O., et al. 2022, *ApJ*, 929, 78
- Pedregosa, F., Varoquaux, G., Gramfort, A., et al. 2011, *Journal of Machine Learning Research*, 12, 2825
- Plotkin, R. M., Anderson, S. F., Brandt, W. N., et al. 2010, *AJ*, 139, 390
- Plotkin, R. M., Shemmer, O., Trakhtenbrot, B., et al. 2015, *The Astrophysical Journal*, 805, 123
- Rankine, A. L., Hewett, P. C., Banerji, M., & Richards, G. T. 2020, *MNRAS*, 492, 4553
- Richards, G. T., McCaffrey, T. V., Kimball, A., et al. 2021, *AJ*, 162, 270
- Richards, G. T., Lacy, M., Storrie-Lombardi, L. J., et al. 2006, *ApJS*, 166, 470
- Richards, G. T., Kruczek, N. E., Gallagher, S. C., et al. 2011, *AJ*, 141, 167
- Rivera, A. B., Richards, G. T., Gallagher, S. C., et al. 2022, *ApJ*, 931, 154
- Rivera, A. B., Richards, G. T., Hewett, P. C., & Rankine, A. L. 2020, *ApJ*, 899, 96
- Robinson, A. 1994, in *Astronomical Society of the Pacific Conference Series*, Vol. 69, *Reverberation Mapping of the Broad-Line Region in Active Galactic Nuclei*, ed. P. M. Gondhalekar, K. Horne, & B. M. Peterson, 147
- Runnoe, J. C., Brotherton, M. S., & Shang, Z. 2012, *MNRAS*, 422, 478
- Shemmer, O., Brandt, W. N., Anderson, S. F., et al. 2009, *ApJ*, 696, 580
- Shemmer, O., Brandt, W. N., Netzer, H., Maiolino, R., & Kaspi, S. 2008, *ApJ*, 682, 81
- Shemmer, O., & Lieber, S. 2015, *ApJ*, 805, 124
- Shemmer, O., Netzer, H., Maiolino, R., et al. 2004, *ApJ*, 614, 547
- Shemmer, O., Brandt, W. N., Schneider, D. P., et al. 2006, *ApJ*, 644, 86
- Shemmer, O., Trakhtenbrot, B., Anderson, S. F., et al. 2010, *ApJL*, 722, L152
- Shen, Y. 2013, *Bulletin of the Astronomical Society of India*, 41, 61
- . 2016, *ApJ*, 817, 55
- Shen, Y., & Ho, L. C. 2014, *Nature*, 513, 210

- Shen, Y., Richards, G. T., Strauss, M. A., et al. 2011, *ApJS*, 194, 45
- Shen, Y., Brandt, W. N., Dawson, K. S., et al. 2015, *ApJS*, 216, 4
- Shen, Y., Brandt, W. N., Richards, G. T., et al. 2016, *ApJ*, 831, 7
- Shen, Y., Wu, J., Jiang, L., et al. 2019, *ApJ*, 873, 35
- Spergel, D. N., Bean, R., Doré, O., et al. 2007, *ApJS*, 170, 377
- Timlin, J. D., Brandt, W. N., Ni, Q., et al. 2020, *MNRAS*, 492, 719
- Tody, D. 1986, in *Society of Photo-Optical Instrumentation Engineers (SPIE) Conference Series*, Vol. 627, *Instrumentation in astronomy VI*, ed. D. L. Crawford, 733
- van der Walt, S., Colbert, S. C., & Varoquaux, G. 2011, *CSE*, 13, 22
- Vanden Berk, D. E., Richards, G. T., Bauer, A., et al. 2001, *AJ*, 122, 549
- Virtanen, P., Gommers, R., Oliphant, T. E., et al. 2020, *Nature Methods*, 17, 261
- Wandel, A., Peterson, B. M., & Malkan, M. A. 1999, *ApJ*, 526, 579
- Wang, Y., Liu, W., Shang, Z., & Brotherton, M. S. 2022, *MNRAS*, 515, 5836
- Wes McKinney. 2010, in *Proceedings of the 9th Python in Science Conference*, ed. Stéfan van der Walt & Jarrod Millman, 56 – 61
- Wright, E. L., Eisenhardt, P. R. M., Mainzer, A. K., et al. 2010, *AJ*, 140, 1868
- Wu, J., Brandt, W. N., Anderson, S. F., et al. 2012, *ApJ*, 747, 10
- Wu, J., Brandt, W. N., Hall, P. B., et al. 2011, *ApJ*, 736, 28
- York, D. G., Adelman, J., Anderson, John E., J., et al. 2000, *AJ*, 120, 1579
- Yu, L.-M., Bian, W.-H., Wang, C., Zhao, B.-X., & Ge, X. 2019, *MNRAS*, 488, 1519
- Yu, L.-M., Bian, W.-H., Zhang, X.-G., et al. 2020a, *ApJ*, 901, 133
- Yu, L.-M., Zhao, B.-X., Bian, W.-H., Wang, C., & Ge, X. 2020b, *MNRAS*, 491, 5881

APPENDIX

A. NIR SPECTROSCOPY OF SDSS J1137+3919
AND SDSS J2137–0039

SDSS J113747.64+391941.5 and SDSS J213742.25–003912.7 (hereafter, SDSS J1137+3919 and SDSS J2137–0039, respectively) are two WLQs with redshifts suitable for observing the $H\beta$ line in the H -Band. Observations of these quasars were carried out by the *Gemini-North* Observatory using GNIRS throughout four observing runs between 2014 March 14 and 2014 August 4, under program GN-2014A-Q-47. The observation log appears in Table A.1. For both targets, we used the Short Blue Camera, with spatial resolution $0.''15 \text{ pix}^{-1}$, and a $1.0''$ slit to achieve a spectral resolution of $R \sim 600$. An H -filter was applied, producing a spectral range of $1.5 - 1.8 \mu\text{m}$, corresponding to rest-frame $\sim 4500 - 5300 \text{ \AA}$. Exposure times for each subintegration were 238 s and 220 s, and the total integration times were 7140 s and 7040 s for SDSS J1137+3919 and SDSS J2137–0039, respectively. These observations were performed using the standard “ABBA” nodding pattern of the targets along the slit in order to obtain primary background subtraction.

The spectra were processed using the standard procedure of the IRAF *Gemini* package based on the PyRAF Python-based interface. Exposures from the same nodding position were added to boost the signal-to-noise ratio, then the sum of exposures from two different nodding positions were subtracted to remove background noise. Wavelength calibration was done against an Argon lamp in order to assign wavelength values to the observed pixels.

Spectra of telluric standard stars with $T_{\text{eff}} \sim 9700 \text{ K}$ were taken immediately before or after the science exposures to remove telluric absorption features in the quasars’ observed spectra. These spectra were processed in a similar fashion, followed by a removal of the stars’ intrinsic hydrogen absorption lines by fitting a Lorentzian profile to each hydrogen absorption line, and interpolating across this feature to connect the continuum on each side of the line. The quasars’ spectra were divided by the corrected stellar spectra. The corrected quasar spectra were then multiplied by an artificial blackbody curve with a temperature corresponding to the telluric standard star, which yielded a cleaned, observed-frame quasar spectrum.

Flux calibrations were obtained by taking the Wide-field Infrared Survey Explorer (WISE; Wright et al. 2010) $W1$ -band (at $3.4 \mu\text{m}$) apparent magnitudes, re-

ported by SDSS Data Release 16 (Lyke et al. 2020), and the $W1$ isophotal flux density $F_{\lambda}(\text{iso})$ given in Table 1 of Jarrett et al. (2011). Flux densities at $3.4 \mu\text{m}$ were derived according to:

$$F_{\lambda}(3.4 \mu\text{m}) = F_{\lambda}(\text{iso}) \cdot 10^{-\text{mag}/2.5}. \quad (\text{A1})$$

The flux densities at $3.4 \mu\text{m}$ were extrapolated to flux densities at $1.63 \mu\text{m}$, roughly corresponding to $\lambda_{\text{rest}} = 5100 \text{ \AA}$, assuming an optical continuum of the form $F_{\nu} \propto \nu^{-0.5}$ (e.g., Vanden Berk et al. 2001).

We modeled the spectra following the methods of Shemmer et al. (2004) and Shemmer et al. (2010). Our model consists of a linear continuum through the average flux densities of two narrow ($\sim 20 \text{ \AA}$) rest-frame bands centered on 4750 \AA and 4975 \AA , a broadened Fe II emission template (Boroson & Green 1992), and two Gaussian profiles for the $H\beta$ $\lambda 4861$ emission-line. No [O III] emission-lines are detectable in either spectrum, and we placed upper limits on their EWs by fitting a Gaussian feature where the [O III] emission-lines should be such that they are indistinguishable from the continuum. The final, calibrated near infrared spectra of the two WLQs appear in Figure A.1.

In both sources we detected weak and relatively narrow $H\beta$ lines as well as strong Fe II features compared to quasars at similar luminosities and redshifts (e.g., see Netzer et al. 2007; Shen 2016). We also determined the systemic redshift (z_{sys}) values from the observed-frame wavelength of the peak (λ_{peak}) of the $H\beta$ emission-line, a similar treatment as in Matthews et al. (2021) for sources that lack [O III] emission. The z_{sys} values are larger than the redshifts reported by Lyke et al. (2020) by $\Delta z = 0.008$ in SDSS J1137+3919 and by $\Delta z = 0.013$ in SDSS J2137–0039, corresponding to velocity offsets (blueshifts) of 700 km s^{-1} and 1184 km s^{-1} , respectively, which is consistent with typical velocity offsets between SDSS Pipeline redshifts and z_{sys} values observed in luminous, high-redshift quasars (Dix et al. 2020, Paper I). The rest-frame spectra in Figure A.1 have henceforth been corrected by z_{sys} . Rest-frame EWs of $H\beta$ $\lambda 4861$, Fe II $\lambda\lambda 4434 - 4684$, and the upper limit on the EWs of [O III] $\lambda 5007$ were calculated for SDSS J1137+3919 to be 16 \AA , 53 \AA , and $\leq 4 \text{ \AA}$, and for SDSS J2137–0039 to be 20 \AA , 49 \AA , and $\leq 5 \text{ \AA}$, respectively. The flux densities at a rest-frame wavelength of 5100 \AA are $7.77 \times 10^{-18} \text{ ergs cm}^{-2} \text{ s}^{-1} \text{ \AA}^{-1}$ and $8.18 \times 10^{-18} \text{ ergs cm}^{-2} \text{ s}^{-1} \text{ \AA}^{-1}$, respectively.

Table A.1. *Gemini-North* GNIRS *H*-Band Observation Log

| Quasar (SDSS J) | z^a | z_{sys}^b | $\log \nu L_\nu(5100 \text{ \AA})$ (erg s^{-1}) | Observation Dates | Exp. Time (s) |
|--------------------|-------|--------------------|---|----------------------|------------------|
| 113747.64+391941.5 | 2.420 | 2.428 | 45.8 | 2014 Mar 14, 20 | 7140 |
| 213742.25-003912.7 | 2.281 | 2.294 | 45.8 | 2014 Jun 29, Aug 04 | 7040 |

^a Obtained from visually-inspected redshifts (z_{vis}) reported in SDSS Data Release 16 (Lyke et al. 2020)

^b Systemic redshifts (see § A for details).

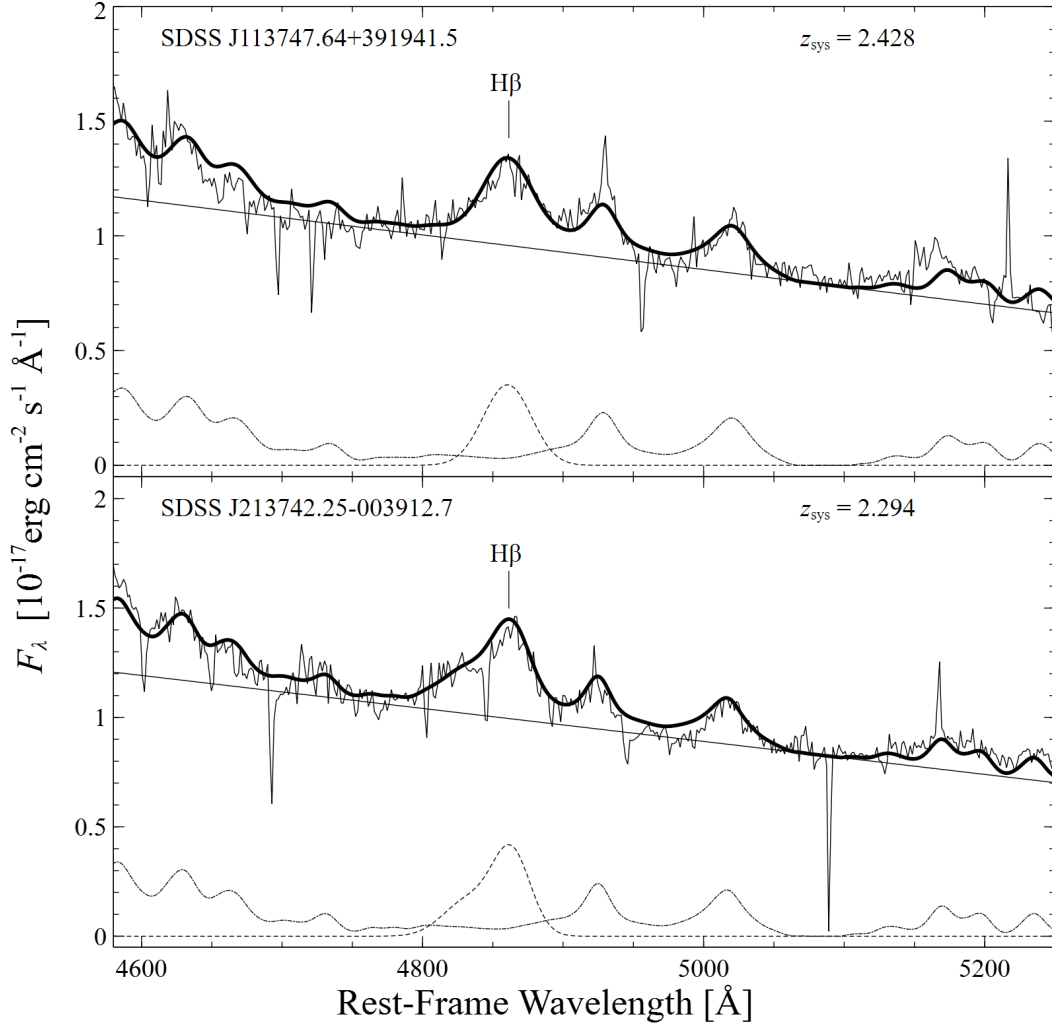


Figure A.1. The NIR spectra of SDSS J1137+3919 (top) and SDSS J2137–0039 (bottom). In each panel, the continuous line is the observed spectrum of each quasar. The continuous straight line below the spectrum is the linear continuum fit. The dashed line is the H β λ 4861 profile modelled with two Gaussians. The dotted-dashed line is the Fe II template from Boroson & Green (1992), which was broadened by 1500 km s $^{-1}$ for SDSS J1137+3919, and 1400 km s $^{-1}$ for J2137–0039. The bold solid line is the entire fitted spectrum.